Neuropharmacology 196 (2021) 108676

Contents lists available at ScienceDirect

Neuropharmacology

journal homepage: www.elsevier.com/locate/neuropharm

(*S*)-[^{18}F]THK5117 brain uptake is associated with Aβ plaques and MAO-B enzyme in a mouse model of Alzheimer's disease

Obada M. Alzghool [a,b,c], Johanna Rokka [a], Francisco R. López-Picón [a,b], Anniina Snellman [a,b], Jatta S. Helin [a,b], Nobuyuki Okamura [d], Olof Solin [a,e,f], Juha O. Rinne [a,g], Merja Haaparanta-Solin [a,b,*]

[a] Turku PET Centre, University of Turku, Kiinamyllynkatu 4-8, FI-20520, Turku, Finland
[b] Medicity Research Laboratory, University of Turku, Tykistökatu 6 A, FI-20520, Turku, Finland
[c] Drug Research Doctoral Programme, University of Turku, Turku, Finland
[d] Division of Pharmacology, Faculty of Medicine, Tohoku Medical and Pharmaceutical University, Sendai, Japan
[e] Department of Chemistry, University of Turku, Vatselankatu 2, FI-20500, Turku, Finland
[f] Accelerator Laboratory, Turku PET Centre, Åbo Akademi University, Kiinamyllynkatu 4-8, FI-20520, Turku, Finland
[g] Division of Clinical Neurosciences, Turku University Hospital, Kiinamyllynkatu 4-8, FI-20520, Turku, Finland

ARTICLE INFO

Keywords:
Alzheimer's disease
APP/PS1-21
Beta-amyloid
MAO-B
(*S*)-[^{18}F]THK5117
Tau

ABSTRACT

The mouse model of beta-amyloid (Aβ) deposition, APP/PS1-21, exhibits high brain uptake of the tau-tracer (*S*)-[^{18}F]THK5117, although no neurofibrillary tangles are present in this mouse model. For this reason we investigated (*S*)-[^{18}F]THK5117 off-target binding to Aβ plaques and MAO-B enzyme in APP/PS1-21 transgenic (TG) mouse model of Aβ deposition. APP/PS1-21 TG and wild-type (WT) control mice in four different age groups (2–26 months) were imaged antemortem by positron emission tomography with (*S*)-[^{18}F]THK5117, and then brain autoradiography. Additional animals were used for immunohistochemical staining and MAO-B enzyme blocking study with deprenyl pre-treatment. Regional standardized uptake value ratios for the cerebellum revealed a significant temporal increase in (*S*)-[^{18}F]THK5117 uptake in aged TG, but not WT, brain. Immunohistochemical staining revealed a similar increase in Aβ plaques but not endogenous hyper-phosphorylated tau or MAO-B enzyme, and *ex vivo* autography showed that uptake of (*S*)-[^{18}F]THK5117 co-localized with the amyloid pathology. Deprenyl hydrochloride pre-treatment reduced the binding of (*S*)-[^{18}F]THK5117 in the neocortex, hippocampus, and thalamus. This study's findings suggest that increased (*S*)-[^{18}F]THK5117 binding in aging APP/PS1-21 TG mice is mainly due to increasing Aβ deposition, and to a lesser extent binding to MAO-B enzyme, but not hyper-phosphorylated tau.

1. Introduction

Tau and beta-amyloid (Aβ) aggregations are the main neuropathological hallmarks of Alzheimer's disease (AD) (LaFerla and Oddo, 2005). Tau is primarily expressed in neuronal axons and to a less extent in somas and dendrites, but is also present in astrocytes and oligodendrocytes (Šimić et al., 2016). In AD, abnormally phosphorylated tau (p-tau) aggregates into paired helical filaments (PHFs) and straight filaments, both of which assemble neurofibrillary tangles (NFTs) in neuronal cell bodies and neuropil threads (NTs) in axons and dendrites (Hasegawa, 2016). NFT and NT aggregation and distribution correlates closely with AD progression (Braak et al., 2006) and clinical symptoms (Bierer et al., 1995), respectively. This evidence referred to a significant role of tau pathology in AD and created strong interest in developing a positron emission tomography (PET) tracer for imaging tau pathology *in vivo*. A validated tau PET tracer could assist in early diagnosis of AD and the evaluation of disease-modifying therapeutics in clinical development.

To date, several tracers have been developed to image tau pathology (Okamura et al., 2014); (Okamura et al., 2018). However, extensive characterization of the first generation tau-targeting tracers, including the most commonly used [^{18}F]flortaucipir (formerly known as [^{18}F]AV1451 and T807) (Xia et al., 2013), [^{11}C]PBB3 (Maruyama et al.,

Abbreviations: Aβ, beta-amyloid; MAO-B, monoamine oxidase B; WT, wild type; TG, transgenic.

* Corresponding author. Turku PET Centre, University of Turku, Tykistökatu 6 A, 4th floor, FI-20520, Turku, Finland.
E-mail address: merja.haaparanta-solin@utu.fi (M. Haaparanta-Solin).

https://doi.org/10.1016/j.neuropharm.2021.108676
Received 24 January 2021; Received in revised form 4 June 2021; Accepted 9 June 2021
Available online 30 June 2021

2013), and THK tracer family ([^{18}F]THK523, [^{18}F]THK5105, [^{18}F]THK5117, [^{18}F]THK5317, [^{18}F]THK5351) (Harada et al., 2016) revealed undesired tracer characteristics, such as off-target binding, mainly to Aβ plaques in the case of [^{18}F]flortaucipir and [^{11}C]PBB3, and monoamine oxidase B (MAO-B) enzyme in the case of the THK tracer family (Leuzy et al., 2019)' (Saint-Aubert et al., 2017). Thus, second generation tau tracers have been developed and are currently being evaluated in clinical settings: [^{18}F]MK6240 by Merck (Betthauser et al., 2019), [^{18}F]RO948 by Roche (Kuwabara et al., 2018), and [^{18}F]GTP-1 by Genentech (Sanabria Bohórquez et al., 2019).

One of the first generation tau tracers in the THK family, [^{18}F]THK5117, binds to tau PHFs based on their β-sheet structure (Harada et al., 2015), labeling intracellular and extracellular NFTs and NFTs located in dystrophic neuritis (aka neuritic plaques), but not pre-tangle formations (Harada et al., 2016);'Okamura et al. (2013);'Lemoine et al. (2015). [^{18}F]THK5117 first reported to have high brain uptake and fast wash-out in healthy mice, and high *in vitro* binding affinity to synthetic tau protein aggregates and tau-rich AD brain homogenates (Okamura et al., 2013). Although the brain distribution of [^{18}F]THK5117 differentiates AD patients from healthy subjects, and cortical tracer binding highlights regions of NFTs with high p-tau (Harada et al., 2015), substantial non-specific binding to white matter is a main drawback of [^{18}F]THK5117 (Harada et al., 2016). The pure *S*-enantiomer of the THK tracer family, ((*S*)-[^{18}F]THK5117), had presented faster washout, improved *in vivo* binding affinity, and reduced non-specific white matter binding compared to the racemic form (Tago et al., 2016a, 2016b). However, the improved version, (*S*)-[^{18}F]THK5117 (also referred to as [^{18}F]THK5317), still suffers from off-target binding to MAO-B enzyme as shown in *in silico* and *in vivo* studies (Murugan et al., 2019). Thus, the clinical applications of (*S*)-[^{18}F]THK5117 are diminished, especially with the arrival of the second-generation tau-targeting tracers.

This present cross-sectional imaging study was initiated to investigate the off-target binding properties of the proposed tau-tracer, (*S*)-[^{18}F]THK5117, towards Aβ plaques and MAO-B enzyme *in vivo*, and tracer's pharmacokinetic properties in the APP/PS1-21 transgenic (TG) mouse model of Aβ deposition (Radde et al., 2006) and wild type (WT) littermates. No NFTs are present in the APP/PS1-21 mouse model, and there is only a minor presence of mouse endogenous p-tau within dystrophic neurites in the vicinity of the Aβ plaques (Radde et al., 2008).

As NFTs and Aβ plaques share similar β-sheet structures (Kirschner et al., 1986), we hypothesized that (*S*)-[^{18}F]THK5117 binds Aβ plaques in the APP/PS1-21 mouse model of Aβ deposition.

2. Materials and methods

2.1. Production of (S)-[^{18}F]THK5117

(*S*)-[^{18}F]THK5117 (6-[(3-[^{18}F]fluoro-2-hydroxy)propoxy]-2-(4-methylaminophenyl)quinoline) was produced in the Radiopharmaceutical Laboratory at the Turku PET Centre using a previously described method (Okamura et al., 2013) with slight modifications. A detailed description of the synthesis is in the Supplementary data. For the 11 synthesis batches of (*S*)-[^{18}F]THK5117, the radiochemical yield was 11 ± 5%, molar activity 840 ± 410 GBq/μmol, radiochemical purity > 98%, and shelf-life 6 h.

2.2. Animals and ethical statement

This study was performed with APP/PS1-21 TG mice from C57BL/6J background (n = 40; 13 females; weight 30.0 ± 4.9 g), and C57BL/6J and littermate WT control mice (n = 25; 9 females; weight 39.0 ± 8.4 g; Supplemental Table 1). PET imaging, brain autoradiography, biodistribution and radiometabolite analysis were performed with TG and WT mice aged 2–26 months. Different groups of mice were selected for immunohistochemical staining between 3 and 23 months of age, and at 10 months for the MAO-B enzyme blocking study. This study was approved by the Animal Experiment Board of the Province of Southern Finland (ESAVI/4660/04.10.07/2016), and performed in accordance with the European Ethics Committee (decree 86/609/CEE) and ARRIVE guidelines.

The APP/PS1-21 TG mouse model of Aβ deposition, a hallmark of AD, co-expresses human APP and PSEN1 with KM670/671NL and L166P mutations, respectively, driven by the neuron-specific mouse Thy1 gene fragment on a C57BL/6J background. Starting at 2 months, this mutant phenotype progressively develops Aβ plaques, which are associated with strong gliosis (Radde et al., 2006). APP/PS1-21 mice were originally provided by KOESLER (Rottenburg, Germany) and further bred with C57BL/6Cn mice and housed in the Central Animal Laboratory of University of Turku according to the guidelines of the International Council of Laboratory Animal Science (ICLAS). Three to four mice of the same gender were housed in each ventilated cage under the following standard conditions: temperature 21 ± 3 °C, humidity 55 ± 15%, 12-h light cycle (7:00 to 19:00 light), aspen wood bedding, and ad libitum access to soy-free chow (RM3 (E) Soya Free, 801710, Special Diets Service, Essex, UK) and tap water.

2.3. In vivo PET/CT imaging and analysis of PET imaging data

PET imaging was performed in TG (n = 23; 6 females) and WT (n = 20; 6 females) mice at 2–3, 6–10, 12–16, and 19–26 months using an Inveon Multimodality PET/CT scanner (Siemens Medical Solutions, Knoxville, TN). Two mice were imaged simultaneously. First, mice were anesthetized by inhaled isoflurane (300 mL/min 3.5% isoflurane/O_2 for induction and 2% for maintenance) and computed tomography (CT) scan was performed for anatomic reference and attenuation correction. Immediately after an intravenous bolus injection of (*S*)-[^{18}F]THK5117 (injected dose 6.0 ± 0.8 MBq, injected mass 154 ± 88 ng/kg, injected volume ≤ 200 μL), dynamic PET was performed for 40 min. During the scans and while under anesthesia, the mice were laid prone on a heating pad and an ophthalmic gel (Oftagel, Santen Oy, Tampere, Finland) used to protect the eyes from drying. After the PET scans, the mice were sacrificed for the *ex vivo* studies.

The 3D list mode PET data were rebinned into 2D sinograms with a Fourier rebinning algorithm, and then reconstructed with a 2D-filtered back-projection algorithm (final voxel size 0.78 × 0.78 × 0.80 mm). Data were divided into 49 time frames (30 × 10, 15 × 60, 4 × 300 s). Data were decay-corrected to the injection time. PET images were analyzed using Inveon Research Workplace analysis software v. 4.2 (Siemens Medical Solutions). A dynamic PET image was co-registered by rigid transformation and rotation with the corresponding reference CT image and a 3D magnetic resonance imaging (MRI) mouse brain template (MRM NAt Mouse Brain Database, McKnight Brain Institute) as an anatomical reference. Brain uptake of (*S*)-[^{18}F]THK5117 was analyzed in the frontal cortex (FC), striatum (STR), thalamus (THA), hypothalamus, hippocampus (HIPPO), neocortex (NC), and cerebellum (CB) on the fused CT image and MRI template. The volumes of interest (VOIs) were drawn for each mouse separately with the help of an MRI template. Almost identical volumes were always used for the analyzed brain regions. Additionally, unintentional bias by the data analyser was avoided as the PET image was used only for the co-registration step of CT image and MRI template and eliminated before the VOIs were drawn. From the VOIs, the regional ^{18}F-radioactivity concentration was acquired as time-activity curves (TACs), and CB-normalized standardized uptake value (SUV) ratios ($SUVR_{CB}$) for the 20–40 min time frame were calculated. Steady-state (*S*)-[^{18}F]THK5117 binding was achieved approximately 20 min after injection.

2.4. Ex vivo brain autoradiography and analysis of digital autoradiography images

Ex vivo brain autoradiography was performed in TG (n = 15; 5 females) and WT (n = 16; 7 females) mice at 2–3, 6–7, 12–16, and 19–26

months. Forty minutes after (S)-[^{18}F]THK5117 injection, mice were sacrificed by cardiac puncture under deep isoflurane anesthesia, followed by transcardial perfusion with saline. The brains were dissected, frozen, and sliced as described previously (Takkinen et al., 2017).

Brain sections were cut on the level of the FC, STR, parietotemporal cortex (PTC), HIPPO, THA, HYPO, pons, and CB. In each mouse, 32 sections were cut from each mentioned region of interest (ROI). Digital autoradiographs were analyzed using Aida Image Analyser v. 4.5 (Raytest Isotopenmessgeräte GmbH, Straubenhardt, Germany). ^{18}F-radioactivity intensity profiles, expressed as background-erased photo-stimulated luminescence per pixel, were drawn manually on $\geq$ 7 sections/ROI/mouse. Regional uptake of (*S*)-[^{18}F]THK5117 was evaluated by calculating the mean ROI_{area}/ROI_{CB} intensity binding ratios.

2.5. MAO-B enzyme blocking study

To evaluate the off-target binding of (*S*)-[^{18}F]THK5117 to MAO-B enzyme, separate groups of 10-month-old TG mice (n = 5 males) were used. The pre-treated group (n = 3) received an intraperitoneal injection (10 mg/kg, 600 μL) of a selective, irreversible inhibitor of MAO-B, (R)-(−)-deprenyl hydrochloride (Selegiline hydrochloride, Sigma-Aldrich), diluted in saline 24 and 1 h before the scans (MacGregor et al., 1985). The control group (n = 2) did not receive any injections. Mice were imaged and sacrificed for *ex vivo* brain autoradiography and immunohistochemical staining as described above.

2.6. Immunohistochemical staining

Separate groups of TG (n = 12; 7 females) and WT (n = 5; 3 females) mice were used to provide supporting histopathological data to the *in vivo* and *ex vivo* imaging studies by immunohistochemical staining. Staining was performed at 3, 7–9, 11–14, and 23 months. Fixed-frozen brain sections were stained for the presence and spatial distribution of Aβ plaques, p-tau, and MAO-B. In addition, fresh-frozen brain sections obtained from mice used in the MAO-B enzyme blocking study were examined for the presence and co-localization of MAO-B and Aβ plaques using immunohistochemical and immunofluorescent double staining. The antibodies and staining protocols are described in Supplemental Table 2.

Stained brain sections were digitized using the Panoramic 250 Flash and Panoramic Midi digital slide scanners (3DHistech, Budapest, Hungary). Images were examined and captured using Case Viewer v. 2.1 (3DHistech). The amount of regional Aβ plaques and p-tau but not MAO-B were quantified in the NC and THA using 2 sections from each mouse. The count of 6E10 or AT8-positive objects/mm^2 as average values for ROI/mouse were calculated using QuPath (Bankhead et al., 2017).

2.7. Ex vivo organ biodistribution

The TG (n = 13; 4 females) and WT (n = 15; 6 females) mice were sacrificed 40 min after injection and cardiac blood (~500 μL) immediately collected in gel-lithium heparin tube (Terumo Europe, Leuven, Belgium). Subsequently, organs of interest were dissected, individually weighed, and measured for ^{18}F-radioactivity. The tail was measured to ensure success of the injection. All measurements were decay-corrected, background radioactivity subtracted, and ^{18}F-radioactivity in each organ quantified as the percentage of injected dose (ID) per gram of tissue (%ID/g).

2.8. Metabolism and radiometabolite analysis

Plasma and brain homogenates were analyzed by radio-thin-layer chromatography (radioTLC) at set time points after (*S*)-[^{18}F]THK5117 injection: 5 min (n = 4; 4 WT; 4 females), 15 min (n = 8; 5 WT; 1 female; 3 TG; 1 female), 30 min (n = 3; 3 WT; 3 males), 45 min (n = 4; 4 WT; 4 females), and 60 min (n = 4; 4 WT; 3 females). The detailed protocol is described in the Supplementary data. Using Aida Image Analyser v. 4.5, the percentage of non-metabolized (*S*)-[^{18}F]THK5117 was calculated from the total ^{18}F-radioactivity in the samples.

2.9. Data analysis and statistical methods

For all data sets, results are reported as mean ± standard deviation (SD). The comparison of (*S*)-[^{18}F]THK5117 brain uptake between TG and WT mice in each age group was performed using the non-parametric Mann-Whitney *U* test. Differences were considered significant when $p < 0.05$. Statistical analyses were performed in GraphPad Prism v. 5.01 (GraphPad Software, San Diego, CA).

3. Results

3.1. In vivo PET/CT imaging

The averaged SUV TACs of (*S*)-[^{18}F]THK5117 showed that (*S*)-[^{18}F]THK5117 crossed the blood-brain barrier and peaked 2 min after injection. In addition, the TACs showed a similar uptake and washout levels in both genotypes, but higher retention in the NC of TG mice compared to WT controls at 12–16 months. (*S*)-[^{18}F]THK5117 uptake reached specific binding equilibrium after approximately 20 min. Therefore, the time frame 20–40 min was used for the $SUVR_{CB}$ calculation. Similar results were obtained in the FC, STR, THA, and HIPPO at 6–10 and 19–21 months. (Fig. 1A and B).

The regional $SUVR_{CB}$ of (*S*)-[^{18}F]THK5117 was significantly higher in the NC, HIPPO, FC, STR and THA ($p = 0.0012$; Fig. 2 and Supplemental Fig. 1), and HYPO ($p = 0.0414$, Supplemental Fig. 1) of 6–10 mo old TG mice (n = 7) compared to their age-matched WT controls (n = 6). In 12–16 and 19–26 mo old groups (n = 6/group) the SUVRs were significantly higher in TG than WT mice in NC ($p = 0.0022$), HIPPO ($p = 0.0022$), FC ($p = 0.0303$), STR ($p = 0.0022$) and THA ($p = 0.0022$) (Fig. 2 and Supplemental Fig. 1) but not in the HYPO (12–16 months $p = 0.6212$, and 19–26 months $p = 0.0931$). (*S*)-[^{18}F]THK5117 uptake seemed to reach its highest level at 12–16 months, plateauing thereafter. $SUVR_{CB}$ remained ~1 in WT controls. The SUVs in the CB of both TG and WT mice indicated minimal uptake, with no significant difference between the genotypes. Therefore, CB was used as a reference region (Supplemental Fig. 2). Regional $SUVR_{CB}$ and corresponding *p* values are reported in Supplemental Table 3.

3.2. Ex vivo brain autoradiography

Consistent with the *in vivo* PET results, increased (*S*)-[^{18}F]THK5117 binding in the cortical and subcortical brain regions was demonstrated in coronal brain sections from APP/PS1-21 mice compared to control mice. Non-specific binding to white matter was low, as expected due to using the *S* stereoisomer of [^{18}F]THK5117 (Fig. 3A). Furthermore, region-to-CB binding ratios showed significantly ($p = 0.0043$) higher (*S*)-[^{18}F]THK5117 uptake in TG mice (n = 6) compared to their age-matched WT controls (n = 5) at 12–16 months in the PTC, HIPPO, FC, STR, THA and PONS (Fig. 3B and C and Supplemental Fig. 3A, B, C and E). In the PTC ($p = 0.0043$), HIPPO ($p = 0.0159$), FC ($p = 0.0095$), STR ($p = 0.0043$), and THA ($p = 0.0079$) the region-to-CB binding ratios were significantly higher in TG (n = 5) than WT (n = 6) mice at 19–26 months (Fig. 3B and C and Supplemental Fig. 3A, B, and C). In the PONS ($p = 0.5368$, Supplemental Fig. 3E), the ratios at 19–26 months did not reach the significance. In the HYPO, the region-to-CB ratios in TG and WT mice did not differ significantly in any studied age group (Supplemental Fig. 3D and Supplemental Table 4). A notable (*S*)-[^{18}F]THK5117 uptake in the ventricular structures including 3rd and lateral ventricles was detected. Interestingly, Brendel and colleagues have noticed similar phenomenon using the [^{18}F]THK5117 tracer in a tau mouse model (Brendel et al., 2016).

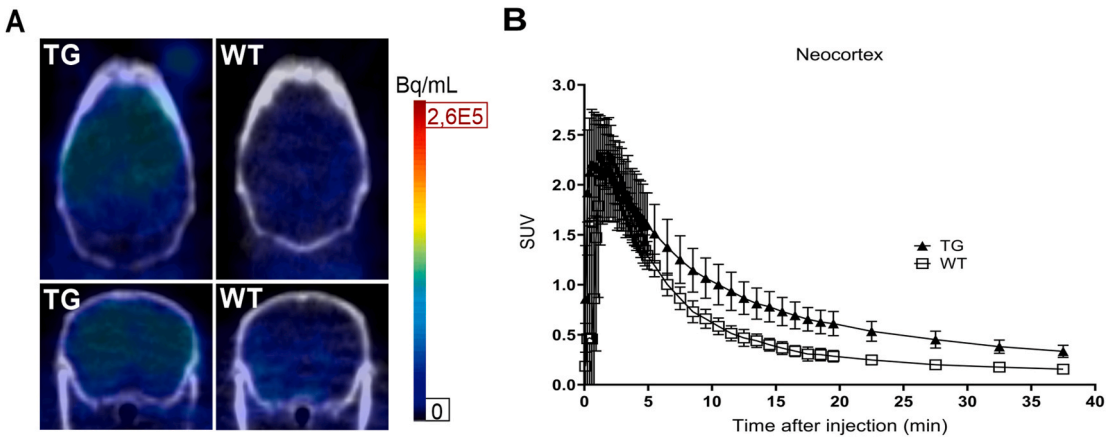

Fig. 1. *In vivo* (*S*)-[^{18}F]THK5117 uptake in transgenic APP/PS1-21 (TG) and wild-type (WT) mouse brain at 12–16 months. (A) Representative PET/CT images of (*S*)-[^{18}F]THK5117 uptake in coronal and axial views summed over 20–40 min. Higher (*S*)-[^{18}F]THK5117 uptake is seen in the fore and midbrain regions of the TG mouse compared to age-matched WT controls at 15 months. No similar uptake pattern was noted in the hindbrain regions, which suggests the cerebellum as a reference region. (B) Averaged SUV time activity curves of (*S*)-[^{18}F]THK5117 in the neocortex of TG mice (n = 6) and age-matched WT controls (n = 6). Note the higher retention in the TG mice. Data are expressed as mean ± standard deviation. SUV = standardized uptake value.

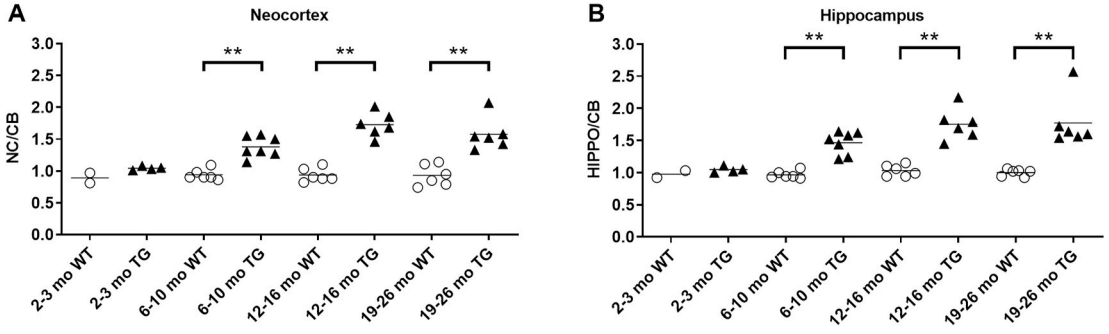

Fig. 2. *In vivo* (*S*)-[^{18}F]THK5117 binding analyzed as $SUV_{region}/SUV_{cerebellum}$ ($SUVR_{CB}$). Significantly higher (*S*)-[^{18}F]THK5117 binding was seen in the neocortex (A) and hippocampus (B) of transgenic APP/PS1-21 (TG) mice compared to age-matched wild-type (WT) controls starting from 6 to 10 months of age. Each symbol represents a different animal. Mann-Whitney *U* test was used to compare intergroup differences between age-matched TG and WT mice: $^{**}p < 0.01$.

3.3. MAO-B enzyme blocking study and immunohistochemical staining

Tracer off-target binding revealed that (*S*)-[^{18}F]THK5117 bound to MAO-B enzyme in the brains of APP/PS1-21 TG mice. Pre-treatment with irreversible MAO-B inhibitor, deprenyl hydrochloride, reduced the binding of (*S*)-[^{18}F]THK5117 in the NC, HIPPO, and THA by 18.2%, 17.3%, and 14.7%, respectively, compared to untreated TG mice of the same gender and age (Fig. 4A). Regional $SUVR_{CB}$ values and corresponding percentage changes in binding are reported in Supplemental Table 5.

Immunohistochemical staining of brain sections from mice used in the MAO-B blocking study revealed similar expression levels of MAO-B enzyme in the deprenyl pre-treated and untreated groups (Fig. 4B) and age-matched WT mice (Supplemental Fig. 4). MAO-B immunoreactivity consistently seemed to appear as either scattered dots or a mild typical astrocyte star-shape in all stained sections. As expected, stained Aβ plaques were abundant in both treated and untreated groups (Fig. 4B), and exhibited similar visual patterns as the brain sections from *ex vivo* brain autoradiography. In addition, fluorescent double staining of Aβ plaques and MAO-B enzyme on the same brain sections used for autoradiography showed the plaques visualized in the autoradiography image (Fig. 4C). Negative control staining was used to verify the antibodies (Supplemental Fig. 4).

3.4. Immunohistochemical staining

In agreement with the imaging results, immunohistochemical staining demonstrated a difference between TG and WT mice in terms of the presence of Aβ plaques and endogenous mouse p-tau in dystrophic neurites. Aβ plaques were detected in the brains of TG mice, in the NC starting at 3 months and increasing in abundance with distribution to all other brain regions up to 23 months. P-tau was detected in cortical and subcortical regions of brains from TG mice starting at 7 months, with mild abundance and no increase relative to Aβ plaques (Fig. 5 and Supplemental Fig. 5). However, NFTs were absent in this TG mouse model.

Quantification of Aβ plaques in NC and THA revealed an increase in plaques count as the TG mice aged with great difference compared to their age-matched WT controls. On the contrary, quantifying p-tau in the same mice revealed a much less prominent increase in p-tau count with aging in TG mice and a very minor difference to their age-matched WT controls (Supplemental Fig. 6). Taken together, the abundance, distribution and quantification of Aβ plaques, but not p-tau, exhibited a similar pattern to (*S*)-[^{18}F]THK5117 PET brain uptake as seen in the PET imaging and autoradiography studies (Figs. 2, 3 and 5 and Supplemental Fig. 6).

3.5. Ex vivo organ biodistribution

The biodistribution of (*S*)-[^{18}F]THK5117-derived ^{18}F-radioactivity

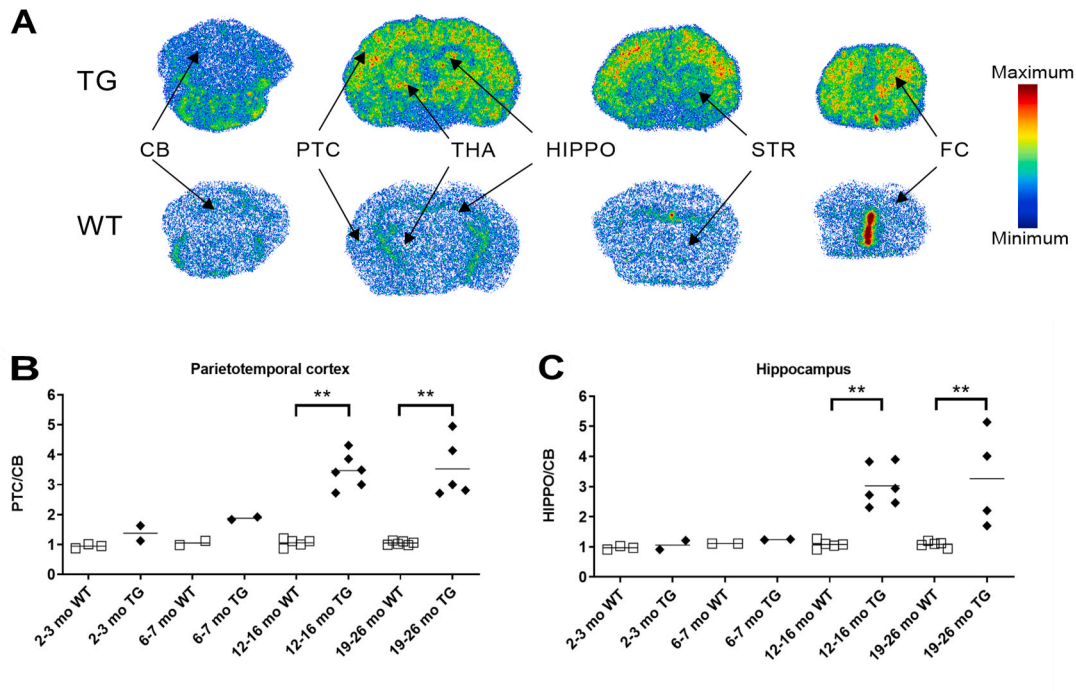

Fig. 3. *Ex vivo* (*S*)-[^{18}F]THK5117 binding in APP/PS1-21 transgenic (TG) and wild-type (WT) mouse brain. (A) Representative coronal brain section autoradiographs obtained from 12-month-old TG and WT mice 40 min after (*S*)-[^{18}F]THK5117 injection. Autoradiographs are adjusted to a similar color scale. (B) Parietotemporal cortex (PTC)-to-cerebellum (CB) ratios are higher in TG mice at 12–16 and 19–26 months than in age-matched WT mice. (C) Hippocampus-to-CB ratios are higher in TG mice than in WT mice at 12–16 and 19–26 months. No change in uptake ratios was seen in WT mice. Each symbol represents a different animal. Mann-Whitney *U* test was used to compare intergroup differences between age-matched TG and WT mice: $^{**}p < 0.01$.

in both TG and WT mice revealed the highest uptake in the liver (6.96 ± 3.32 %ID/g), small intestine (48.94 ± 25.80 %ID/g), eyes (10.25 ± 3.31 %ID/g) and Harderian glands (2.61 ± 1.18 %ID/g), but low in parietal bone (0.19 ± 0.09 %ID/g (Supplemental Table 6).

3.6. Metabolism and radiometabolite analysis

Chromatograms of plasma samples from TG and WT mice (n = 23, 2–26 months) revealed that (*S*)-[^{18}F]THK5117 plasma metabolism was fast and increased as a function of time. Thirty minutes after injection (n = 3, male, WT mice), 45 ± 10.3% of the total plasma ^{18}F-radioactivity originated from unchanged (*S*)-[^{18}F]THK5117. In the same mice, after 30 min, 92.7 ± 4% of the total ^{18}F-radioactivity in the brain originated from unchanged (*S*)-[^{18}F]THK5117.

The plasma sample shows one polar radio-metabolite of (*S*)-[^{18}F]THK5117, whereas the brain sample shows minor peak that could originate from the remaining blood in the brain after the animal is sacrificed (Fig. 6 and Supplemental Fig. 7).

4. Discussion

This study was initiated after we observed high (*S*)-[^{18}F]THK5117 brain uptake in the APP/PS1-21 TG mouse model of Aβ deposition, though an absence of NFTs was previously reported in this model (Radde et al., 2008). Thus, in this cross-sectional imaging study, we investigated the binding selectivity and pharmacokinetic properties of (*S*)-[^{18}F]THK5117 in TG mice and their WT littermates.

A clear temporal increase in (*S*)-[^{18}F]THK5117 *in vivo* uptake was present in the brains of TG mice as they aged. A similar phenomenon was not seen in the WT mice. *In vivo* $SUVR_{CB}$ demonstrated higher regional (*S*)-[^{18}F]THK5117 binding in TG mice compared to their age-matched WT mice. Immunostaining revealed that regional uptake of (*S*)-[^{18}F]THK5117 was associated with Aβ plaques. Antibody 6E10, which recognizes amino acid residues 1–16 of Aβ, immunostaining in the brain of aging TG mice showed a similar temporal increase in Aβ plaques, whereas AT8, which recognizes amino acid residues Ser202/Thr205 of p-tau, immunostaining did not show a similar increase in endogenous p-tau in dystrophic neurites (Supplemental Fig. 6). In addition, *ex vivo* brain (*S*)-[^{18}F]THK5117 autoradiographs of TG mice brain showed similar plaque-like aggregates co-localizing with Aβ plaque staining. Amyloid pathology is already present at 2 months of age in APP/PS1-21 mice and increases with aging (Radde et al., 2006). We also observed this in the present study. The immunohistochemical staining showed that P-tau level in the APP/PS1-21 brain is very low, and was only detected starting at 7 months and remained constant when the animals aged.

Having several age groups allowed us to closely follow the binding trend of (*S*)-[^{18}F]THK5117 with age. APP/PS1-21 mice at 2–3 months had similar (*S*)-[^{18}F]THK5117 binding as age-matched WT controls, which can be explained by the low level of amyloid pathology at this age. In addition, APP/PS1-21 mice ≥12 months old had either plateaued or decreased (*S*)-[^{18}F]THK5117 binding. This was unexpected considering that a temporal increase in amyloid pathology with aging was reported in this mouse model up to 19 months (Radde et al., 2006). This phenomenon is most likely related to individual variation between the mice. Previous research with the APP/PS1-21 mouse model showed that when mice are aging there is a plateau and variability in the detection of AD-pathology using PET tracers (López-Picón et al., 2018).

In vivo SUVs, autoradiographs, and immunohistochemical staining in brains from TG and WT mice demonstrated that CB is a suitable reference region for calculating (*S*)-[^{18}F]THK5117 regional SUVR. These results are in line with Aβ plaque pathology development in this mouse model (Radde et al., 2006). Furthermore, an Aβ plaque radiotracer, [^{18}F]AV-45, has been reported to not exhibit specific binding in the CB of APP/PS1-21 TG mice (Poisnel et al., 2012). As expected, when using the pure (*S*) stereoisomer of the tracer, autoradiography images revealed low (*S*)-[^{18}F]THK5117 off-target binding in the white matter.

Development of (*S*)-[^{18}F]THK5117 for imaging tau pathology

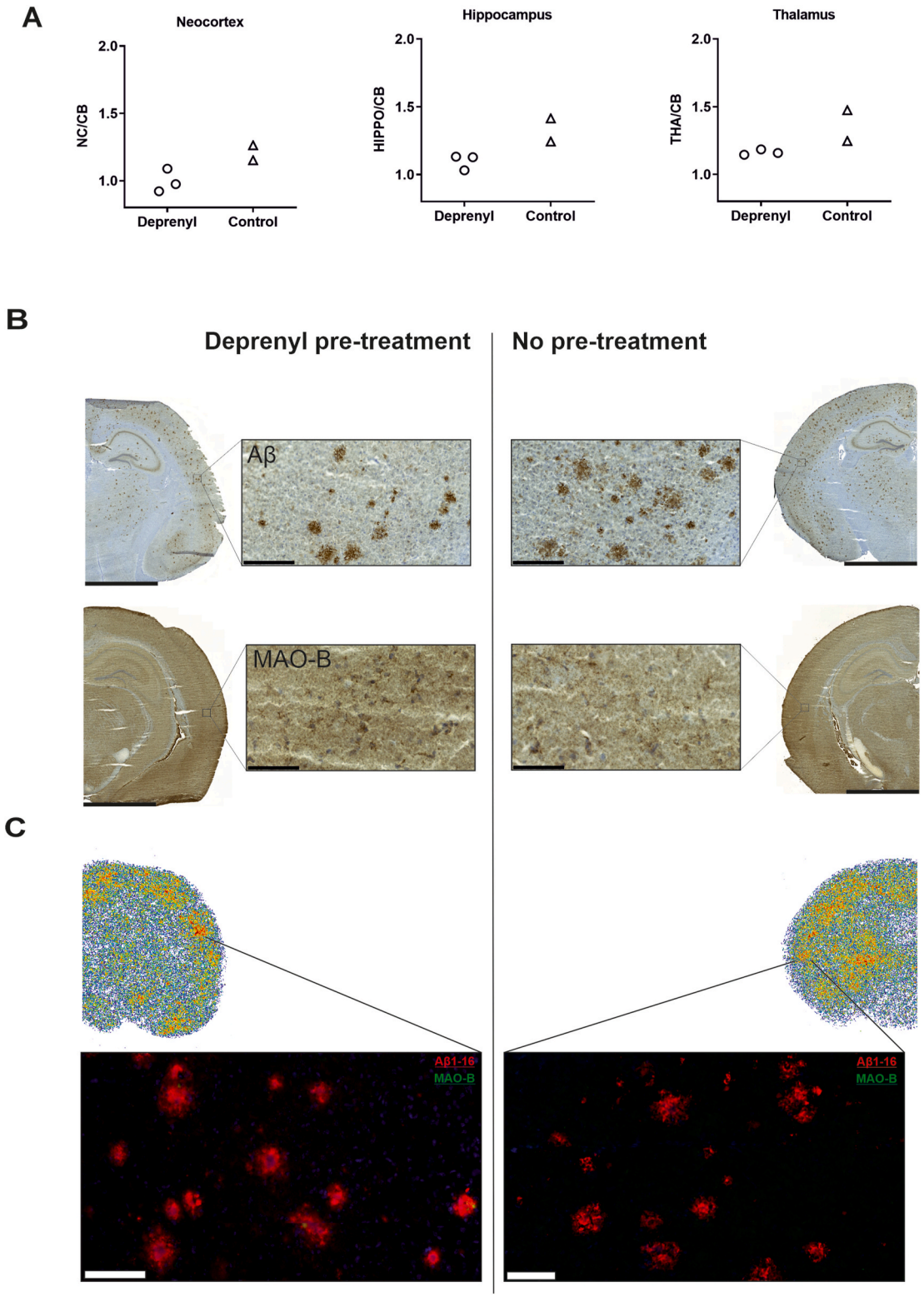

Fig. 4. MAO-B enzyme blocking study. (A) (*S*)-[^{18}F]THK5117 uptake as $SUV_{region}/SUV_{cerebellum}$ ($SUVR_{CB}$) in the neocortex (NC), hippocampus (HIPPO), and thalamus (THA) of deprenyl -treated (n = 3, 10 mg/kg, i.p.) and untreated (n = 2) age-matched transgenic APP/PS1-21 (TG) mice. (B) Immunohistochemical staining of beta-amyloid (Aβ) plaques and MAO-B in the same TG mice. Aβ plaques and MAO-B were stained in consecutive brain sections. (C) Brain autoradiography (ARG) section reveals (*S*)-[^{18}F]THK5117 binding to the Aβ plaques. Fluorescent double staining of Aβ plaques and MAO-B enzyme was performed on the same brain section as ARG. Scale bars = 1000 μm for the hemisphere brain section image, 50 μm for the cortical image. Image enhancement as colour brightness and contrast adjustments have been done to Fig. 4C in order to improve the figure readability.

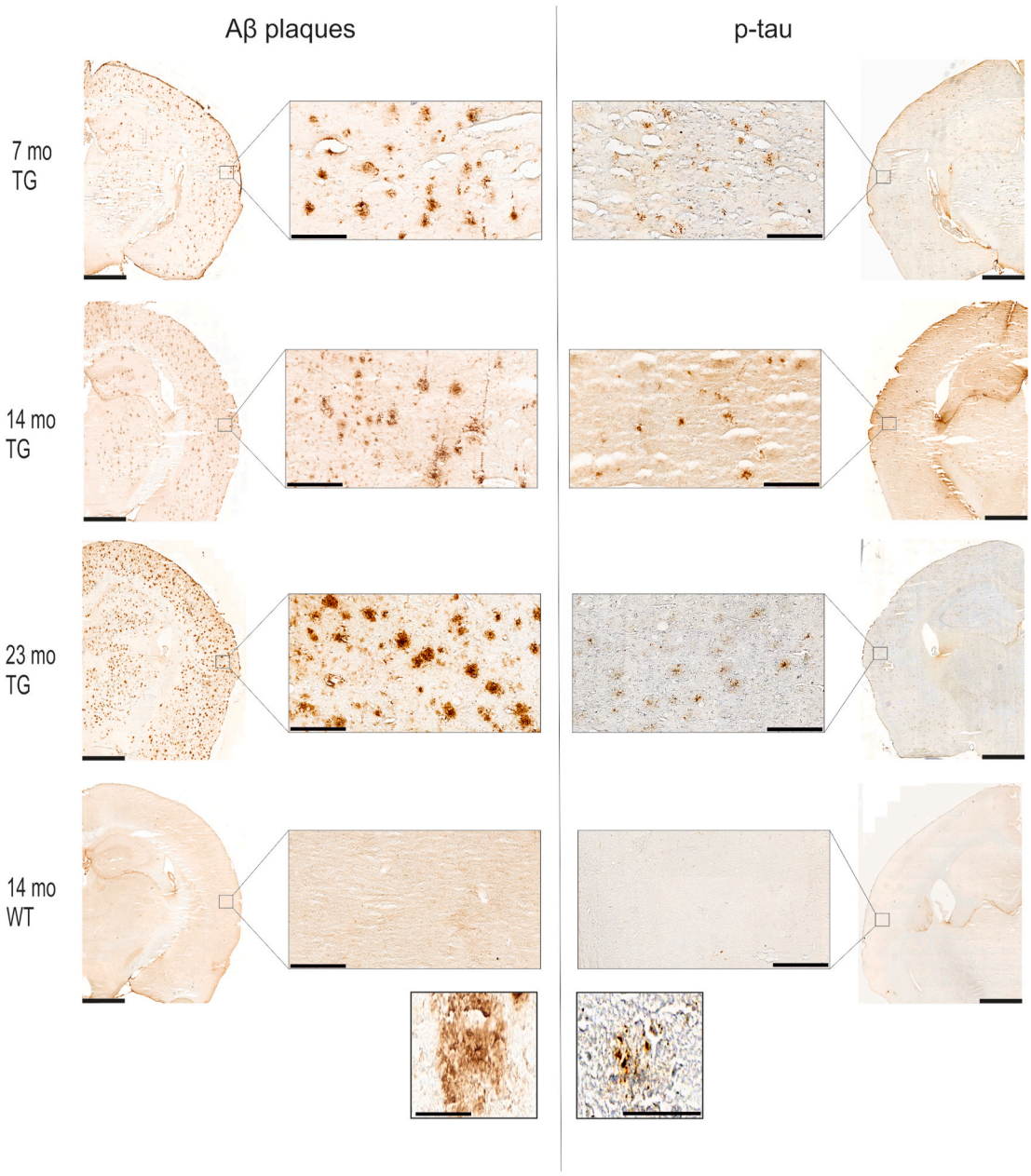

Fig. 5. Immunohistochemical staining study. Beta-amyloid (Aβ) plaques and phosphorylated-tau (p-tau) stained using $Aβ_{1-16}$ and AT8 antibodies in different age groups. In transgenic APP/PS1-21 (TG) mice, Aβ plaques increased as the mice aged. Endogenous mouse p-tau increased slightly in dystrophic neurites. Brain sections from wild-type (WT) control mice showed no signs of pathology. In each age group, Aβ plaque and p-tau were stained using consecutive brain sections from the same animal. The magnified images were taken from TG brain at 23 months. Scale bars = 500 μm for the hemisphere brain section image, 50 μm for the cortical image, 10 μm for the magnified images.

focused on *in vitro* binding assays and autoradiography (Lemoine et al., 2015), and the tracer has been used in patients and healthy subjects (Okamura et al., 2014)'; Ishiki et al., 2015). Our study is the first to investigate (*S*)-[^{18}F]THK5117 binding selectivity in an AD mouse model expressing only Aβ pathology. Two PET studies with the [^{18}F]THK5117 tracer have been published with mouse models of tau pathology. In the first study, $SUVR_{CB}$ revealed higher [^{18}F]THK5117 binding in the brains of TG tau mouse models compared to WT controls *in vivo*, and the results correlated with *ex vivo* and *in vitro* [^{18}F]THK5117 autoradiography, as well as tau AT8 immunohistochemical staining (Brendel et al., 2016). In the second study, [^{18}F]THK5117 was compared longitudinally with [^{18}F]T807 in a tau TG mouse model. Although [^{18}F]THK5117 showed less sensitivity to tau pathology than [^{18}F]T807, [^{18}F]THK5117 revealed fast brain washout and higher $SUVR_{CB}$ in tau TG mice compared to WT controls, which also correlated with tau AT8 immunohistochemical staining (Brendel et al., 2018).

The main obstacle to developing a tau-selective radiotracer is *in vivo* binding selectivity, considering that both p-tau and Aβ plaques are predominantly made of and share similar β-sheet structures, and (*S*)-[^{18}F]THK5117 binding to NFTs depends only on the β-sheet structure, not the tau isoform or the phosphorylation state (Harada et al., 2016). Moreover, in human AD brain, Aβ plaques and NFTs co-localize with a 5 to 20-times higher concentration of Aβ plaques (Agdeppa et al., 2001). Different AD mouse models are known to develop Aβ deposits that differ relative to each other, to human Aβ, and to their ability to bind Aβ -targeted PET ligands, such as [^{11}C]PiB (Snellman et al., 2013). Therefore, we could speculate that the differences observed in the binding specificity of (*S*)-[^{18}F]THK5117 in humans and the APP/PS1-21 mouse

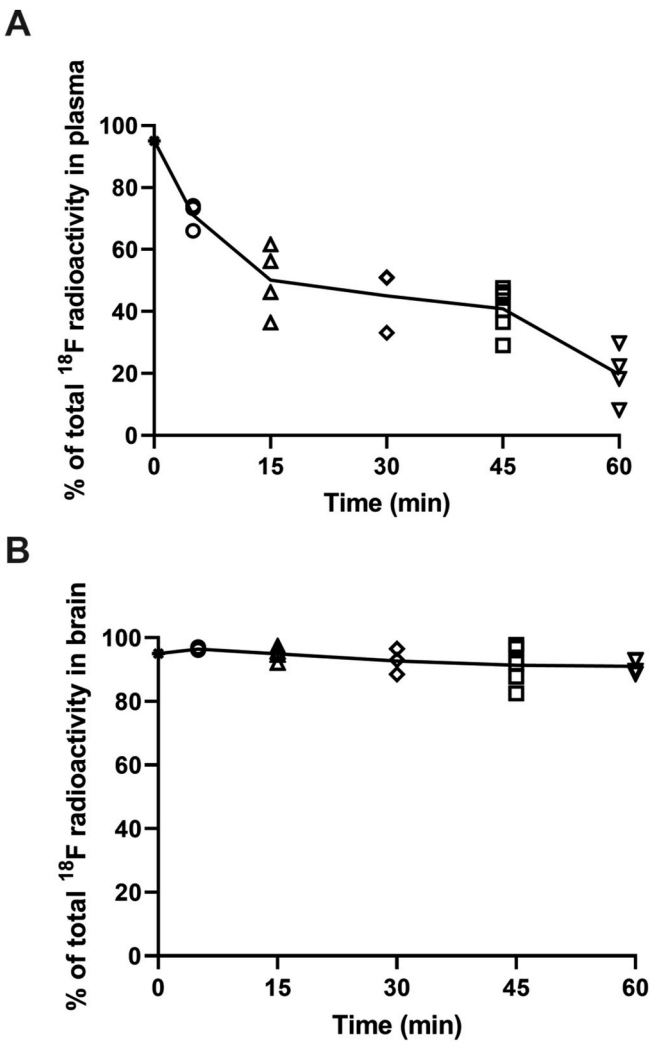

Fig. 6. Fraction of unchanged (*S*)-[^{18}F]THK5117 as a percentage of total ^{18}F-radioactivity in plasma and brain samples from both transgenic APP/PS1-21 (TG) and wild-type (WT) mice (n = 23) measured by radio-thin-layer chromatography (radio-TLC) 5, 15, 30, 45, and 60 min after (*S*)-[^{18}F]THK5117 injection (n ≥ 3/time point). Data are expressed as mean ± standard deviation.

model used in this study could be due to differences in the structure of the Aβ deposits expressed in AD patients and APP/PS1-21 mice.

MAO-B is a ubiquitous enzyme expressed on the outer mitochondrial membrane of astrocytes and serotonergic neurons (Levitt et al., 1982). In the course of AD, MAO-B level can be elevated as part of the neuroinflammatory response (Carter et al., 2012). Previous work with the tritium-labeled THK5117 referred to MAO-B off-target binding. In an *in vitro* autoradiography study on AD brain sections, [^{3}H]THK5117 and [^{3}H]deprenyl exhibited similar binding patterns, which were further validated by immunohistochemical staining. However, the same study revealed minor competition between [^{3}H]THK5117 and unlabeled deprenyl, as well as [^{3}H]deprenyl and unlabeled THK5117, which suggests that THK5117 does not bind MAO-B (Lemoine et al., 2017a). Another related study showed that THK5117 competed with [^{3}H]deprenyl in an *in vitro* binding assay on AD brain homogenate. The authors attributed this discrepancy to differences in technique between *in vitro* autoradiography versus binding assay with the homogenate having more binding sites exposed for binding (Lemoine et al., 2017b). We wanted to investigate whether part of the (*S*)-[^{18}F]THK5117 *in vivo* signal belongs to MAO-B off-target binding in a pharmacological blocking study. To the best of our knowledge, the present study is the first to assess (*S*)-[^{18}F]THK5117 *in vivo* off-target binding to MAO-B enzyme in an AD animal model. Previous PET studies have shown irreversible MAO-B inhibition following administration of a single dose of ^{11}C-labeled MAO-B inhibitors clorgyline and L-deprenyl (Fowler et al., 1987). Our results show that pharmacological blocking of MAO-B enzyme with deprenyl hydrochloride in TG mice was feasible and resulted in reduced (*S*)-[^{18}F]THK5117 binding, which confirms the off-target component towards MAO-B enzyme. In addition, (*S*)-[^{18}F]THK5117 binding was high in TG brain regions with known high level of MAO-B enzyme expression, such as the HIPPO, THA, and cortex. This could be attributed to upregulated MAO-B enzyme expression and increased activity in the APP/PS1-21 mouse model (Jo et al., 2014). Another tracer in the THK family, [^{18}F]THK5351, also demonstrates *in vivo* off-target binding to MAO-B enzyme in the human brain; deprenyl (Selegiline) pre-treatment reduced SUV brain uptake by 36.7–51.8% in various brain regions and was confirmed with autoradiography in a previous study (Ng et al., 2017).

The high brain uptake and fast clearance observed in our study were in line with previous findings using [^{18}F]THK5117 in normal ICR mice (Okamura et al., 2013). The biodistribution of (*S*)-[^{18}F]THK5117 indicated high peripheral uptake of ^{18}F-radioactivity in the gallbladder and intestine, suggesting excretion via the hepatobiliary route. Low ^{18}F-radioactivity in the parietal bone 40 min after injection revealed that the ^{18}F-labeling position is stable and no defluorination occurred *in vivo*. After 60 min p.i. about 60% of total radioactivity originated from the parent compound in plasma and 95% in brain tissue. Thus, the metabolic rate in mice is of the same order of magnitude as Mairinger et al. found in male rats and faster than that found in female rats (Mairinger et al., 2020). Thus, contrary to Mairinger et al. we found no difference in the metabolic rate between sexes.

The study has some limitations that should be considered when interpreting our results. First, the low number of animals (n = 2–7/genotype/age group) limited more robust statistical analyses of the *in vivo* PET and *ex vivo* brain autoradiography data. Second, tau staining was not possible with the same fresh frozen brains used for autoradiography to allow a comparison of (*S*)-[^{18}F]THK5117 binding and p-tau expression on the same sections. However, another set of mice was used in which brains were dissected following perfusion fixation with 4% PFA to gain this information.

5. Conclusion

In this study, we showed that increased (*S*)-[^{18}F]THK5117 binding in aging APP/PS1-21 mice is mainly due to increasing Aβ plaques, and to a lesser extent due to binding to MAO-B enzyme, but not p-tau. Additionally, we can conclude that there are limitations in utilizing (*S*)-[^{18}F]THK5117 for *in vivo* visualization and quantification of NFTs. Further studies in other mouse models of amyloid deposition are needed to confirm the binding selectivity of (*S*)-[^{18}F]THK5117 to Aβ plaques. Our finding highlights the importance of preclinical *in vivo* evaluation of novel PET tracers when the investigated pathology present in animal models resembles that of diseased human brain.

Data availability

The datasets generated during and/or analyzed during the study are available from the corresponding author upon reasonable request.

Author contributions

OA, FRL-P, JR, OS, and MH-S: Conceptualization, methodology NO: Resources; JR: Resources, validation OA, FRL-P, JSH, AS, and MH-S: Investigation OA: Writing - Original Draft, OA, FRL-P, JR, JSH, AS, NO, JOR, OS, and MH-S: Writing- Reviewing and Editing.

Declaration of competing interest

The authors declare no potential conflicts of interest with respect to the research, authorship, and/or publication of this article.

Acknowledgments

We acknowledge the Preclinical Imaging Laboratory personnel for assisting with the studies, the Accelerator Laboratory personnel for radionuclide production, and the staff of Central Animal Laboratory of the University of Turku for assistance with the animal studies.

This work was funded by the Drug Research Doctoral Program at the University of Turku. Prof. Rinne received grants from Sigrid Juselius Foundation, Academy of Finland (project 310962), and state funding for university-level health research (project 13464) during the conduct of the study. Dr. Haaparanta-Solin received a grant from state funding for university-level health research (project 13250); Drs. Haaparanta-Solin and Solin received a grant from the Swedish Cultural Foundation in Finland during the conduct of the study. Prof. Solin received a grant from the Academy of Finland (project 266891 and 334310).

Appendix A. Supplementary data

Supplementary data to this article can be found online at https://doi.org/10.1016/j.neuropharm.2021.108676.

References

Agdeppa, E.D., Kepe, V., Liu, J., Flores-Torres, S., Satyamurthy, N., Petric, A., Cole, G.M., Small, G.W., Huang, S.C., Barrio, J.R., 2001. Binding characteristics of radiofluorinated 6-dialkylamino-2-naphthylethylidene derivatives as positron emission tomography imaging probes for beta-amyloid plaques in Alzheimer's disease. J. Neurosci. 21, RC189. https://doi.org/10.1523/JNEUROSCI.21-24-J0004.2001.

Bankhead, P., Loughrey, M.B., Fernández, J.A., Dombrowski, Y., McArt, D.G., Dunne, P. D., McQuaid, S., Gray, R.T., Murray, L.J., Coleman, H.G., James, J.A., Salto-Tellez, M., Hamilton, P.W., 2017. QuPath: open source software for digital pathology image analysis. Sci. Rep. 7, 1–7. https://doi.org/10.1038/s41598-017-17204-5.

Betthauser, T.J., Cody, K.A., Zammit, M.D., Murali, D., Converse, A.K., Barnhart, T.E., Stone, C.K., Rowley, H.A., Johnson, S.C., Christian, B.T., 2019. In vivo characterization and quantification of neurofibrillary tau PET radioligand 18F-MK-6240 in humans from Alzheimer disease dementia to young controls. J. Nucl. Med. 60, 93–99. https://doi.org/10.2967/jnumed.118.209650.

Bierer, L.M., Carlin, L., Schmeidler, J., Davis, K.L., Hof, P.R., Purohit, D.P., Perl, D.P., 1995. Neocortical neurofibrillary tangles correlate with dementia severity in alzheimer's disease. Arch. Neurol. 52, 81–88. https://doi.org/10.1001/archneur.1995.00540250089017.

Braak, H., Alafuzoff, I., Arzberger, T., Kretzschmar, H., Tredici, K., 2006. Staging of Alzheimer disease-associated neurofibrillary pathology using paraffin sections and immunocytochemistry. Acta Neuropathol. 112, 389–404. https://doi.org/10.1007/s00401-006-0127-z.

Brendel, M., Jaworska, A., Probst, F., Overhoff, F., Korzhova, V., Lindner, S., Carlsen, J., Bartenstein, P., Harada, R., Kudo, Y., Haass, C., Van Leuven, F., Okamura, N., Herms, J., Rominger, A., 2016. Small-animal PET imaging of tau pathology with 18F-THK5117 in 2 transgenic mouse models. J. Nucl. Med. 57, 792–798. https://doi.org/10.2967/jnumed.115.163493.

Brendel, M., Yousefi, B.H., Blume, T., Herz, M., Focke, C., Deussing, M., Peters, F., Lindner, S., von Ungern-Sternberg, B., Drzezga, A., Bartenstein, P., Haass, C., Okamura, N., Herms, J., Yakushev, I., Rominger, A., 2018. Comparison of 18F-T807 and 18F-THK5117 PET in a mouse model of tau pathology. Front. Aging Neurosci. 10, 174. https://doi.org/10.3389/fnagi.2018.00174.

Carter, S.F., Schöll, M., Almkvist, O., Wall, A., Engler, H., Långström, B., Nordberg, A., 2012. Evidence for astrocytosis in prodromal alzheimer disease provided by 11C-deuterium-L-deprenyl: a multitracer PET paradigm combining 11C-Pittsburgh compound B and 18F-FDG. J. Nucl. Med. 53, 37–46. https://doi.org/10.2967/jnumed.110.087031.

Fowler, J.S., MacGregor, R.R., Wolf, A.P., Arnett, C.D., Dewey, S.L., Schlyer, D., Christman, D., Logan, J., Smith, M., Sachs, H., Aquilonius, S.M., Bjurling, P., Halldin, C., Hartvig, P., Leenders, K.L., Lundqvist, H., Oreland, L., Stålnacke, C.G., Långström, B., 1987. Mapping human brain monoamine oxidase a and B with 11C-labeled suicide inactivators and PET. Science 235 (4787), 481–485. https://doi.org/10.1126/science.3099392.

Harada, R., Okamura, N., Furumoto, S., Furukawa, K., Ishiki, A., Tomita, N., Hiraoka, K., Watanuki, S., Shidahara, M., Miyake, M., Ishikawa, Y., Matsuda, R., Inami, A., Yoshikawa, T., Tago, T., Funaki, Y., Iwata, R., Tashiro, M., Yanai, K., Arai, H., Kudo, Y., 2015. [18F]THK-5117 PET for assessing neurofibrillary pathology in Alzheimer's disease. Eur. J. Nucl. Med. Mol. Imag. 42, 1052–1061. https://doi.org/10.1007/s00259-015-3035-4.

Harada, R., Okamura, N., Furumoto, S., Tago, T., Yanai, K., Arai, H., Kudo, Y., 2016. Characteristics of tau and its ligands in PET imaging. Biomolecules. https://doi.org/10.3390/biom6010007.

Hasegawa, M., 2016. Molecular mechanisms in the pathogenesis of alzheimer's disease and Tauopathies-Prion-Like seeded aggregation and phosphorylation. Biomolecules. https://doi.org/10.3390/biom6020024.

Ishiki, A., Okamura, N., Furukawa, K., Furumoto, S., Harada, R., Tomita, N., Hiraoka, K., Watanuki, S., Ishikawa, Y., Tago, T., Funaki, Y., Iwata, R., Tashiro, M., Yanai, K., Kudo, Y., Arai, H., 2015. Longitudinal assessment of Tau pathology in patients with Alzheimer's disease using [18F]THK-5117 positron emission tomography. PloS One 10, e0140311. https://doi.org/10.1371/journal.pone.0140311.

Jo, S., Yarishkin, O., Hwang, Y.J., Chun, Y.E., Park, M., Woo, D.H., Bae, J.Y., Kim, T., Lee, J., Chun, H., Park, H.J., Lee, D.Y., Hong, J., Kim, H.Y., Oh, S.J., Park, S.J., Lee, H., Yoon, B.E., Kim, Y., Jeong, Y., Shim, I., Bae, Y.C., Cho, J., Kowall, N.W., Ryu, H., Hwang, E., Kim, D., Lee, C.J., 2014. GABA from reactive astrocytes impairs memory in mouse models of Alzheimer's disease. Nat. Med. https://doi.org/10.1038/nm.3639.

Kirschner, D.A., Abraham, C., Selkoe, D.J., 1986. X-ray diffraction from intraneuronal paired helical filaments and extraneuronal amyloid fibers in Alzheimer disease indicates cross-beta conformation. Proc. Natl. Acad. Sci. Unit. States Am. 83, 503–507. https://doi.org/10.1073/pnas.83.2.503.

Kuwabara, H., Comley, R.A., Borroni, E., Honer, M., Kitmiller, K., Roberts, J., Gapasin, L., Mathur, A., Klein, G., Wong, D.F., 2018. Evaluation of 18F-RO-948 PET for quantitative assessment of tau accumulation in the human brain. J. Nucl. Med. 59, 1877–1884. https://doi.org/10.2967/jnumed.118.214437.

LaFerla, F.M., Oddo, S., 2005. Alzheimer's disease: aβ, tau and synaptic dysfunction. Trends Mol. Med. https://doi.org/10.1016/j.molmed.2005.02.009.

Lemoine, L., Gillberg, P.G., Svedberg, M., Stepanov, V., Jia, Z., Huang, J., Nag, S., Tian, H., Ghetti, B., Okamura, N., Higuchi, M., Halldin, C., Nordberg, A., 2017a. Comparative binding properties of the tau PET tracers THK5117, THK5351, PBB3, and T807 in postmortem Alzheimer brains. Alzheimer's Res. Ther. 9, 96. https://doi.org/10.1186/s13195-017-0325-z.

Lemoine, L., Saint-Aubert, L., Marutle, A., Antoni, G., Eriksson, J.P., Ghetti, B., Okamura, N., Nennesmo, I., Gillberg, P.G., Nordberg, A., 2015. Visualization of regional tau deposits using 3H-THK5117 in Alzheimer brain tissue. Acta Neuropathol. Commun. 3, 40. https://doi.org/10.1186/s40478-015-0220-4.

Lemoine, L., Saint-Aubert, L., Nennesmo, I., Gillberg, P.G., Nordberg, A., 2017b. Cortical laminar tau deposits and activated astrocytes in Alzheimer's disease visualised by 3H-THK5117 and 3H-deprenyl autoradiography. Sci. Rep. 7, 45496. https://doi.org/10.1038/srep45496.

Leuzy, A., Chiotis, K., Lemoine, L., Gillberg, P.G., Almkvist, O., Rodriguez-Vieitez, E., Nordberg, A., 2019. Tau PET imaging in neurodegenerative tauopathies—still a challenge. Mol. Psychiatr. 1 https://doi.org/10.1038/s41380-018-0342-8.

Levitt, P., Pintar, J.E., Breakefield, X.O., 1982. Immunocytochemical demonstration of monoamine oxidase B in brain astrocytes and serotonergic neurons. Proc. Natl. Acad. Sci. U.S.A. 79, 6385–6389. https://doi.org/10.1073/pnas.79.20.6385.

López-Picón, F.R., Snellman, A., Eskola, O., Helin, S., Solin, O., Haaparanta-Solin, M., Rinne, J.O., 2018. Neuroinflammation appears early on PET imaging and then plateaus in a mouse model of Alzheimer disease. J. Nucl. Med. 59, 509–515. https://doi.org/10.2967/jnumed.117.197608.

MacGregor, R.R., Halldin, C., Fowler, J.S., Wolf, A.P., Arnett, C.D., Langström, B., Alexoff, D., 1985. Selective, irreversible in vivo binding of [11C]clorgyline and [11C]-L-deprenyl in mice: potential for measurement of functional monoamine oxidase activity in brain using positron emission tomography. Biochem. Pharmacol. 34, 3207–3210. https://doi.org/10.1016/0006-2952(85)90173-X.

Mairinger, S., Filip, T., Sauberer, M., Flunkert, S., Wanek, T., Stanek, J., Furtner, S., Hutter-Paier, B., Okamura, N., Kuntner, C., 2020. Plasma pharmacokinetic and metabolism of [18F]THK-5317 are dependent on sex. Nucl. Med. Biol. 84 (85), 28–32. https://doi.org/10.1016/j.nucmedbio.2020.01.001.

Maruyama, M., Shimada, H., Suhara, T., Shinotoh, H., Ji, B., Maeda, J., Zhang, M.R., Trojanowski, J.Q., Lee, V.M.-Y., Ono, M., Masamoto, K., Takano, H., Sahara, N., Iwata, N., Okamura, N., Furumoto, S., Kudo, Y., Chang, Q., Saido, T.C., Takashima, A., Lewis, J., Jang, M.K., Aoki, I., Ito, H., Higuchi, M., 2013. Imaging of tau pathology in a tauopathy mouse model and in alzheimer patients compared to normal controls. Neuron 79, 1094–1108. https://doi.org/10.1016/j.neuron.2013.07.037.

Murugan, N.A., Chiotis, K., Rodriguez-Vieitez, E., Lemoine, L., Ågren, H., Nordberg, A., 2019. Cross-interaction of tau PET tracers with monoamine oxidase B: evidence from in silico modelling and in vivo imaging. Eur. J. Nucl. Med. Mol. Imag. 46, 1369–1382. https://doi.org/10.1007/s00259-019-04305-8.

Ng, K.P., Pascoal, T.A., Mathotaarachchi, S., Therriault, J., Kang, M.S., Shin, M., Guiot, M.C., Guo, Q., Harada, R., Comley, R.A., Massarweh, G., Soucy, J.P., Okamura, N., Gauthier, S., Rosa-Neto, P., 2017. Monoamine oxidase B inhibitor, selegiline, reduces 18F-THK5351 uptake in the human brain. Alzheimer's Res. Ther. 9, 25. https://doi.org/10.1186/s13195-017-0253-y.

Okamura, N., Furumoto, S., Harada, R., Tago, T., Yoshikawa, T., Fodero-Tavoletti, M., Mulligan, R.S., Villemagne, V.L., Akatsu, H., Yamamoto, T., Arai, H., Iwata, R., Yanai, K., Kudo, Y., 2013. Novel 18F-labeled arylquinoline derivatives for noninvasive imaging of tau pathology in alzheimer disease. J. Nucl. Med. 54, 1420–1427. https://doi.org/10.2967/jnumed.112.117341.

Okamura, N., Harada, R., Furumoto, S., Arai, H., Yanai, K., Kudo, Y., 2014. Tau PET imaging in alzheimer's disease. Curr. Neurol. Neurosci. Rep. https://doi.org/10.1007/s11910-014-0500-6.

Okamura, N., Harada, R., Ishiki, A., Kikuchi, A., Nakamura, T., Kudo, Y., 2018. The development and validation of tau PET tracers: current status and future directions. Clin. Transl. Imaging. https://doi.org/10.1007/s40336-018-0290-y.

Poisnel, G., Dhilly, M., Moustié, O., Delamare, J., Abbas, A., Guilloteau, D., Barré, L., 2012. PET imaging with [18F]AV-45 in an APP/PS1-21 murine model of amyloid plaque deposition. Neurobiol. Aging 33, 2561–2571. https://doi.org/10.1016/j.neurobiolaging.2011.12.024.

Radde, R., Bolmont, T., Kaeser, S.A., Coomaraswamy, J., Lindau, D., Stoltze, L., Calhoun, M.E., Jäggi, F., Wolburg, H., Gengler, S., Haass, C., Ghetti, B., Czech, C., Hölscher, C., Mathews, P.M., Jucker, M., 2006. Aβ42-driven cerebral amyloidosis in transgenic mice reveals early and robust pathology. EMBO Rep. 7, 940–946. https://doi.org/10.1038/sj.embor.7400784.

Radde, R., Duma, C., Goedert, M., Jucker, M., 2008. The value of incomplete mouse models of Alzheimer's disease. Eur. J. Nucl. Med. Mol. Imag. 35, 70–74. https://doi.org/10.1007/s00259-007-0704-y.

Saint-Aubert, L., Lemoine, L., Chiotis, K., Leuzy, A., Rodriguez-Vieitez, E., Nordberg, A., 2017. Tau PET imaging: present and future directions. Mol. Neurodegener. https://doi.org/10.1186/s13024-017-0162-3.

Sanabria Bohórquez, S., Marik, J., Ogasawara, A., Tinianow, J.N., Gill, H.S., Barret, O., Tamagnan, G., Alagille, D., Ayalon, G., Manser, P., Bengtsson, T., Ward, M., Williams, S.P., Kerchner, G.A., Seibyl, J.P., Marek, K., Weimer, R.M., 2019. [18F]GTP1 (Genentech Tau Probe 1), a radioligand for detecting neurofibrillary tangle tau pathology in Alzheimer's disease. Eur. J. Nucl. Med. Mol. Imag. 46, 2077–2089. https://doi.org/10.1007/s00259-019-04399-0.

Šimić, G., Babić Leko, M., Wray, S., Harrington, C., Delalle, I., Jovanov-Milošević, N., Bažadona, D., Buée, L., de Silva, R., Giovanni, G., Di Wischik, C., Hof, P.R., 2016. Tau protein hyperphosphorylation and aggregation in alzheimer's disease and other tauopathies, and possible neuroprotective strategies. Biomolecules. https://doi.org/10.3390/biom6010006.

Snellman, A., López-Picón, F.R., Rokka, J., Salmona, M., Forloni, G., Scheinin, M., Solin, O., Rinne, J.O., Haaparanta-Solin, M., 2013. Longitudinal amyloid imaging in mouse brain with 11C-PIB: comparison of APP23, Tg2576, and APPswe-PS1dE9 mouse models of Alzheimer disease. J. Nucl. Med. 54, 1434–1441. https://doi.org/10.2967/jnumed.112.110163.

Tago, T., Furumoto, S., Okamura, N., Harada, R., Adachi, H., Ishikawa, Y., Yanai, K., Iwata, R., Kudo, Y., 2016a. Preclinical evaluation of [18F]THK-5105 enantiomers: effects of chirality on its effectiveness as a tau imaging radiotracer. Mol. Imag. Biol. 18, 258–266. https://doi.org/10.1007/s11307-015-0879-8.

Tago, T., Furumoto, S., Okamura, N., Harada, R., Adachi, H., Ishikawa, Y., Yanai, K., Iwata, R., Kudo, Y., 2016b. Structure-activity relationship of 2-arylquinolines as PET imaging tracers for tau pathology in alzheimer disease. J. Nucl. Med. 57, 608–614. https://doi.org/10.2967/jnumed.115.166652.

Takkinen, J.S., López-Picón, F.R., Al Majidi, R., Eskola, O., Krzyczmonik, A., Keller, T., Löyttyniemi, E., Solin, O., Rinne, J.O., Haaparanta-Solin, M., 2017. Brain energy metabolism and neuroinflammation in ageing APP/PS1-21 mice using longitudinal 18F-FDG and 18F-DPA-714 PET imaging. J. Cerebr. Blood Flow Metabol. 37, 2870–2882. https://doi.org/10.1177/0271678X16677990.

Xia, C.F., Arteaga, J., Chen, G., Gangadharmath, U., Gomez, L.F., Kasi, D., Lam, C., Liang, Q., Liu, C., Mocharla, V.P., Mu, F., Sinha, A., Su, H., Szardenings, A.K., Walsh, J.C., Wang, E., Yu, C., Zhang, W., Zhao, T., Kolb, H.C., 2013. [18F]T807, a novel tau positron emission tomography imaging agent for Alzheimer's disease. Alzheimer's Dementia 9, 666–676. https://doi.org/10.1016/j.jalz.2012.11.008.